

HFBRI-MAE: Handcrafted Feature Based Rotation-Invariant Masked Autoencoder for 3D Point Cloud Analysis

Xuanhua Yin, Dingxin Zhang, Jianhui Yu, Weidong Cai
School of Computer Science, The University of Sydney
{xyin0811, dzha2344, jianhui.yu, tom.cai}@sydney.edu.au

Abstract—Self-supervised learning (SSL) has demonstrated remarkable success in 3D point cloud analysis, particularly through masked autoencoders (MAEs). However, existing MAE-based methods lack rotation invariance, leading to significant performance degradation when processing arbitrarily rotated point clouds in real-world scenarios. To address this limitation, we introduce Handcrafted Feature-Based Rotation-Invariant Masked Autoencoder (HFBRI-MAE), a novel framework that refines the MAE design with rotation-invariant handcrafted features to ensure stable feature learning across different orientations. By leveraging both rotation-invariant local and global features for token embedding and position embedding, HFBRI-MAE effectively eliminates rotational dependencies while preserving rich geometric structures. Additionally, we redefine the reconstruction target to a canonically aligned version of the input, mitigating rotational ambiguities. Extensive experiments on ModelNet40, ScanObjectNN, and ShapeNetPart demonstrate that HFBRI-MAE consistently outperforms existing methods in object classification, segmentation, and few-shot learning, highlighting its robustness and strong generalization ability in real-world 3D applications.

Index Terms—3D Point Cloud, Rotation Invariance, Masked Autoencoder

I. INTRODUCTION

The point cloud is a widely used representation of 3D data [1], which plays a crucial role in fields that require real-world perception, such as autonomous driving [2], medical data processing [3], [4], and robotics [5]. In recent years, there have been increasing attempts to apply cutting-edge self-supervised learning (SSL) frameworks to 3D point cloud recognition [6]–[16]. As unlabeled 3D data is vastly more plentiful compared to fully annotated data, SSL approaches exploit pre-training on unlabeled data, reducing annotation costs while simultaneously enhancing performance in downstream tasks [6]. This demonstrates the high potential and application value of SSL in point cloud research.

Among all SSL methods, the reconstruction-based Masked Autoencoder (MAE) [11]–[13] has shown remarkable effectiveness and applicability in point cloud analysis. By reconstructing masked point patches using partially visible ones, MAE enables the extracted features to align well with the local geometry and global context information required for point cloud recognition. However, existing studies remain largely confined to laboratory conditions where objects are aligned

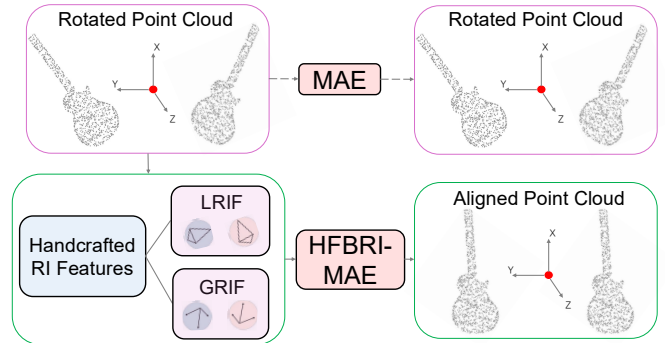


Fig. 1: Comparison between standard MAE and HFBRI-MAE under rotated point clouds. HFBRI-MAE uses handcrafted rotation-invariant features and aligned reconstruction targets to achieve consistent features learning across rotations.

in fixed canonical poses, neglecting the arbitrary rotations encountered in real-world scenarios. Rotation-invariant models are inherently resistant to the effects of point cloud rotations, enabling them to capture rotation-invariant features more effectively and handle complex rotational variations with greater accuracy. Conventional MAE models, even with extensive data augmentation, experience significant performance degradation when encountering randomly rotated point clouds, often performing much worse than supervised models specifically designed for rotation invariance [17]–[21], [23]–[30].

To address this limitation, we propose an enhancement to existing MAE models that retains the advantages of SSL while achieving rotation invariance. A well-established approach in self-supervised rotation-invariant point cloud models involves leveraging handcrafted features based on rotation-invariant line segments and angle information [18], [19]. We hypothesize that it is possible to build a rotation-invariant MAE model by leveraging handcrafted features as input, as rotational information is eliminated before data are fed into the model. In addition, the MAE patch masking and reconstruction mechanism forces the model to infer missing patch information from visible patches, making it well-suited for learning high-quality hidden inter-patch local and intra-patch global rotation-

invariant representations for 3D point clouds. Both token embedding and position embedding procedures can be effectively implemented using these handcrafted features. One challenge of this approach is that MAE relies on known information to infer missing data, therefore losing orientation cues may disrupt this inference process. To mitigate this, we propose a carefully balanced strategy incorporating handcrafted feature design, optimal mask ratios, and well-calibrated encoder-decoder architecture to ensure the pretrained model extracts high-quality features.

Building on these insights, we introduce the **H**andcrafted **F**eature-**B**ased **R**otation-**I**nvariant **M**asked **A**utoencoder (HFBRI-MAE). As shown in Fig. 1, HFBRI-MAE eliminates rotational information from input by integrating rotation-invariant local features (RILF) and rotation-invariant global features (RIGF). Specifically, RILF captures fine-grained geometric details for token embedding, while RIGF encodes spatial relationships among patches for position embedding. These handcrafted features incorporate comprehensive rotation-invariant distance and angle information, enriching the feature space and enhancing the model’s ability to capture intricate geometric structures. Additionally, the rotational information in the output should also be removed, so we align the target reconstructed point cloud with a canonical pose, ensuring that the entire network focuses exclusively on reconstructing rotation-invariant features. Experimental results demonstrate that HFBRI-MAE consistently outperforms existing methods across diverse tasks, including classification, segmentation, and few-shot learning. These findings underscore its ability to extract rotation-invariant features and highlight its adaptability for various 3D point cloud applications. The main contributions of this work are summarized as follows:

- We propose HFBRI-MAE, a novel point cloud SSL framework that integrates rotation-invariant handcrafted features with masked autoencoder, ensuring consistency across varying orientations.
- The framework incorporates RILF and RIGF, capturing both fine-grained geometric details and holistic spatial relationships to improve representation quality.
- Extensive experiments on benchmark datasets demonstrate the effectiveness of HFBRI-MAE outperforms state-of-the-art methods across multiple downstream tasks, including object classification, segmentation, and few-shot learning.

II. RELATED WORKS

A. Deep Learning in Point Cloud

Deep learning has revolutionized 3D point cloud analysis through two dominant paradigms: MLP-based methods [31]–[33] and attention-based architectures [34], [36]. The pioneering work of PointNet [31] introduced point-wise MLPs and max-pooling to aggregate global features but struggled to capture fine-grained local geometric details. This limitation was partially addressed by PointNet++ [32], which employed

hierarchical feature learning through point down-sampling. Attention-based methods, such as PCT [34] and Point Transformer [36], further advanced the field by modeling dynamic point relationships. PCT leverages global self-attention for comprehensive context capture, while Point Transformer focuses on local neighborhoods to balance computational efficiency. In parallel, CurveNet [35] introduced curve-based feature aggregation to enhance local geometric continuity. Recent advancements like PointNeXt [33] integrate lightweight MLP designs with advanced data augmentations, achieving scalability and state-of-the-art performance.

B. Rotation-Invariant Point Cloud Analysis

Achieving rotation invariance remains a critical challenge for real-world 3D applications. Early efforts include handcrafted methods such as RICov [18], which encodes local geometric relationships to construct rotation-invariant features, and its improved variant RICov++ [19], which introduces global features for enhanced robustness. Alternative approaches like GCANet [20], LGR-Net [21] and Yu et al. [22] rely on local reference frames (LRFs) to align point coordinates, while PaRI-Conv [23] and PaRot [24] disentangle pose information from geometric features. PCA-based methods [25], [26] align point clouds into canonical poses but suffer from sign ambiguities and instability under noise. Equivariant models, such as Tensor Field Network [27] and SE(3)-Transformer [28], leverage spherical harmonics and attention mechanisms to ensure feature consistency across SE(3) transformations, offering theoretically guaranteed rotation invariance.

C. Self-Supervised Learning for Point Clouds

In self-supervised learning (SSL), contrastive methods like PointContrast [6] and CrossPoint [7] learn representations by contrasting positive and negative pairs, though their reliance on precise alignment limits robustness. Clustering-based approaches [8] group points into semantic clusters but struggle with 3D data variability. Reconstruction-based methods, including FoldingNet [9] and PSG-Net [10], focus on structural relationships, while PointMAE [11] and PointM2AE [12] extend masked autoencoders (MAEs) to reconstruct masked regions. However, these methods lack inherent rotation invariance. Recent attempts like MaskLRF [13] integrate LRFs for rotation invariance but incur prohibitive computational overhead, and RI-MAE [14] adopts PCA-based alignment but remains sensitive to noise and point density variations.

Our work addresses these gaps by integrating rotation-invariant handcrafted features into the MAE framework. Unlike LRF-based methods, the proposed HFBRI-MAE avoids computational bottlenecks, and compared to PCA-based approaches, it eliminates instability caused by noisy alignments, achieving robust performance under arbitrary rotations.

III. METHODOLOGY

A. Problem Description

Rotation invariance (RI) is essential for practical 3D point cloud analysis, as real-world objects can appear in arbitrary

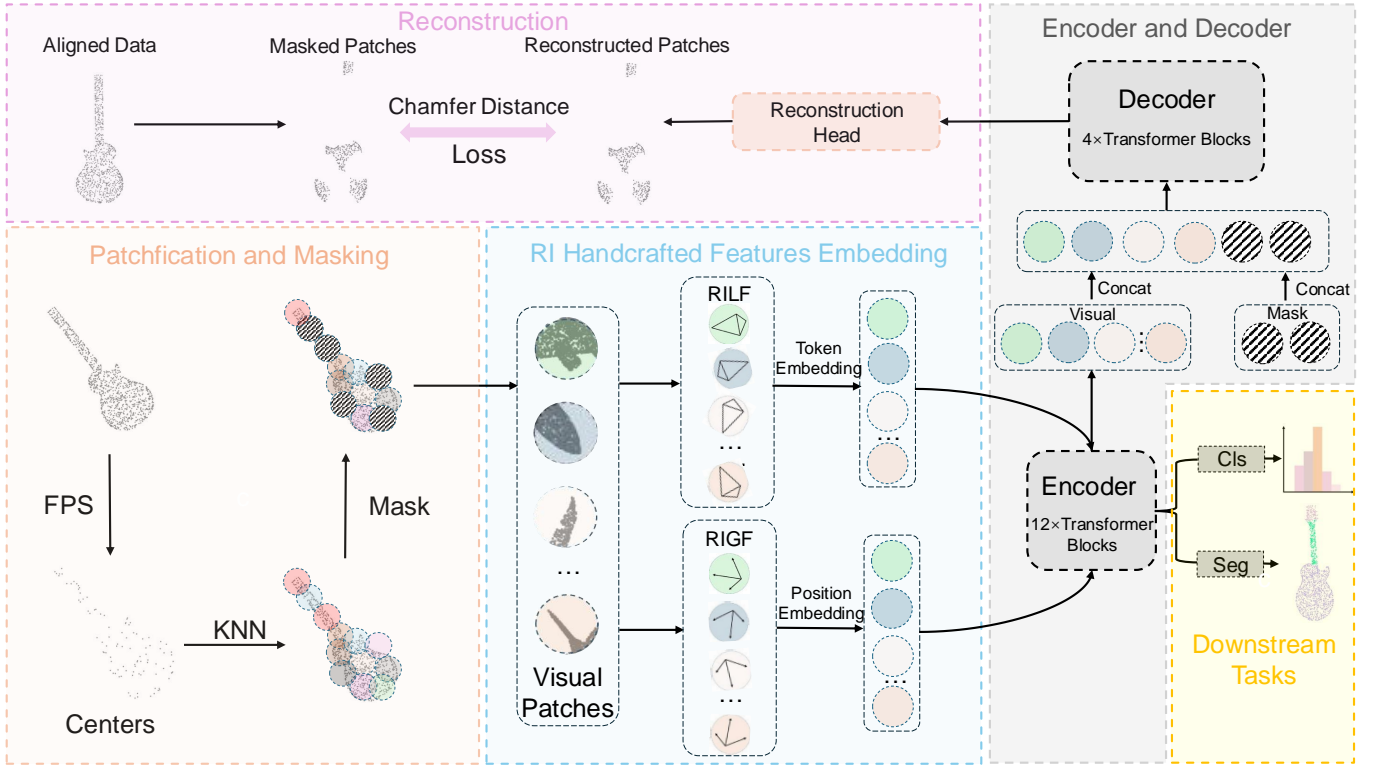


Fig. 2: Architecture of the proposed HF Bri-MAE framework. The input point cloud is divided into patches using FPS and KNN. RILF and RIGF are extracted to form token and position embeddings, which are processed by the encoder. The decoder reconstructs masked patches using aligned point cloud coordinates, facilitating self-supervised learning and downstream tasks.

orientations. Formally, a model is rotation-invariant if its feature encoder f satisfies:

$$f(\mathbf{P}) = f(\mathbf{R}\mathbf{P}), \quad \forall \mathbf{R} \in \text{SO}(3), \mathbf{P} \in \mathbb{R}^{N \times 3}, \quad (1)$$

where \mathbf{P} denotes the input point cloud and \mathbf{R} is a rotation matrix in $\text{SO}(3)$, the group of all proper 3D rotation matrices.

Building upon Eq. 1, we propose Rotation-Invariant Handcrafted Features (RIHF) to encode geometric features (e.g., distances, angles) that are invariant to rotations. The input point cloud \mathbf{P} is decomposed into K local patches $\{\mathbf{P}_i\}_{i=1}^K$ via Farthest Point Sampling (FPS) for centroid selection and k -Nearest Neighbors (KNN) for neighborhood construction. During pretraining, a subset of patches is randomly masked as reconstruction targets. For each unmasked patch \mathbf{P}_i , RIHF enforces rotation invariance by:

$$\text{RIHF}(\mathbf{P}_i) = \text{RIHF}(\mathbf{R}\mathbf{P}_i), \quad \forall \mathbf{R} \in \text{SO}(3). \quad (2)$$

The extracted features are transformed into token embeddings that encode local geometric patterns and position embeddings that maintain spatial relationships. These embeddings are then fed into the encoder to learn high-level geometric features.

However, the strict rotation invariance of RIHF creates a fundamental challenge for reconstruction tasks. Since RIHF produces identical features for \mathbf{P} and $\mathbf{R}\mathbf{P}$, the decoder g receives the same input features regardless of how the point

cloud is rotated. This leads to an inherent ambiguity: the decoder cannot determine whether the original input was rotated or not.

To resolve this ambiguity, we redefine the reconstruction target as the aligned point cloud $\mathbf{P}_{\text{align}} = \text{Align}(\mathbf{R}\mathbf{P})$, which removes the rotational component through coordinate normalization. The reconstruction objective therefore becomes:

$$g(\text{RIHF}(\mathbf{R}\mathbf{P})) = g(\text{RIHF}(\mathbf{P})) \rightarrow \mathbf{P}_{\text{align}}. \quad (3)$$

The key insight is that while the decoder cannot recover the original rotated instance \mathbf{P} as the orientation information has been eliminated, it can reliably reconstruct the rotation-normalized geometry $\mathbf{P}_{\text{align}}$. This approach maintains rotation invariance in feature learning while providing a well-posed reconstruction target.

B. HF Bri-MAE Architecture

The proposed HF Bri-MAE framework extends the MAE architecture, as depicted in Fig. 2. The input point cloud $\mathbf{P} \in \mathbb{R}^{N \times 3}$ is first decomposed into N_p patches. This process begins with FPS to select patch centroids $\{\mathbf{p}_i\}_{i=1}^{N_p}$ that maximize spatial coverage. Subsequently, KNN grouping is applied to form local neighborhoods. This two-stage approach ensures the preservation of both fine-grained local details and global structural context.

During the pretraining phase, we mask a high ratio subset of patches (50%–80%) by replacing them with learnable

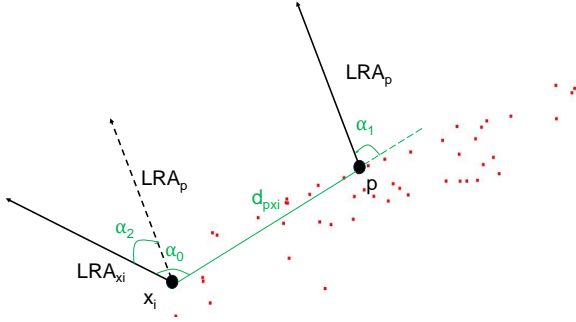


Fig. 3: Visualization of distance features (d_{pxi}) and angle relationships with reference point ($\alpha_0, \alpha_1, \alpha_2$) in RILF.

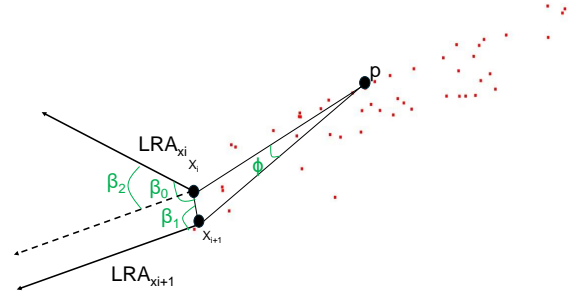


Fig. 4: Visualization of inter-neighbor angle relationship ($\phi, \beta_0, \beta_1, \beta_2$) in RILF.

embedding tokens. The visible patches are first converted to RIHF, then converted to embeddings through designed embedding networks. Although adopting a fixed masking strategy facilitates training stability and implementation simplicity, it may limit the model’s adaptability to varying input structures. In contrast, adaptive masking—guided by factors such as geometric complexity or local feature density—offers a potential pathway to enhance the model’s flexibility and representation learning capacity. Investigating such dynamic masking strategies remains an important direction for future research. The encoder f processes these invariant embeddings to generate latent representations. A decoder g then reconstructs the masked patches from these latent features, employing efficient self-attention mechanisms to minimize computational overhead.

For downstream finetuning, the masking mechanism is disabled to utilize the complete point cloud input. The pretrained encoder remains fixed while task-specific heads are appended for applications such as classification and segmentation.

C. Rotation-Invariant Handcrafted Features (RIHF)

Our designed RIHF consists of two complementary components to achieve more complete rotation invariance: Rotation-Invariant Local Features (RILF) that capture fine-grained geometric patterns within local patches, and Rotation-Invariant Global Features (RIGF) that encode broader structural relationships across spatial regions.

Rotation-Invariant Local Features (RILF). We develop RILF, building upon RConv++’s concepts [19], with all features designed within local patches. Our framework incorporates three feature types: distance feature, reference point angle features, and inter-neighbor angle features. Surface normal vectors are commonly used as stable geometric references for constructing rotation-invariant features. However, many point cloud datasets lack explicit normal vectors, necessitating the development of alternative approaches.

We address this limitation by introducing the Local Reference Axis (LRA), derived from the smallest eigenvector of the local neighborhood’s covariance matrix. Points are projected onto the tangent plane at the reference point p , and ordered clockwise, starting from the farthest point to

maintain consistent point ordering relationships under arbitrary rotations.

The distance feature (d_{pxi}) quantifies the spatial proximity between neighboring points and the reference point p , as illustrated in Fig. 3. The reference point angle features ($\alpha_0, \alpha_1, \alpha_2$) represent the angle relationships between the target point x_i and the reference point p , including the LRA and connecting vectors. The inter-neighbor angle features ($\phi, \beta_0, \beta_1, \beta_2$) encode the angle relationships between adjacent points x_i and x_{i+1} , as shown in Fig. 4.

We construct the comprehensive RILF by concatenating these geometric features:

$$\text{RILF}(x_i) = [d_{pxi}, \alpha_0, \alpha_1, \alpha_2, \phi, \beta_0, \beta_1, \beta_2]. \quad (4)$$

Rotation-Invariant Global Features (RIGF). We propose RIGF to encode global spatial relationships using a neighborhood ball-based structure centered on the reference point p . Each ball corresponds exactly to the patch represented by the reference point, containing all the points within that patch. The ball’s radius r is determined by the farthest point from the reference point within the patch [29]. As illustrated in Fig. 5, we define point m as the centroid of the ball and point s as the intersection between the ball boundary and the ray extending from the origin to reference point p . The RIGF incorporates three distance measurements (d_p, d_{pm}, d_{sm}) and two global angle features (α, β). d_p measures the origin-to- p distance, d_{pm} measures the p -to- m distance, and d_{sm} measures the s -to- m distance. The angles α and β quantify the relationships between vectors \vec{pm} , \vec{ps} , and \vec{ms} . The complete RIGF representation is formulated as:

$$\text{RIGF}(pi) = [d_p, d_{pm}, d_{sm}, \alpha, \beta]. \quad (5)$$

D. Encoder and Decoder

To effectively process the RIHF, we enhance the MAE’s encoder-decoder framework with three key components: embedding layers that transform RILF and RIGF into higher-dimensional representations, a transformer-based encoder for feature processing, and a decoder for point cloud reconstruction.

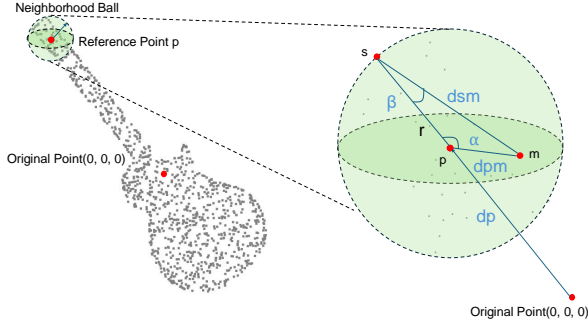


Fig. 5: Visualisation of the RIGF ($d_p, d_{pm}, d_{sm}, \alpha, \beta$) construction process using the neighborhood ball, which is centered at the reference point p with a radius r defined by the distance to the farthest neighboring point.

Embedding. The embedding process transforms RIHF into higher-dimensional representations required by the encoder-decoder architecture. This transformation operates through two parallel pathways. RILF undergo mapping to token embeddings through a Multi-Layer Perceptron (MLP), which yield the representation in encoder space:

$$\mathbf{E}_{\text{token}} = \text{MLP}_{\text{local}}(\text{RILF}). \quad (6)$$

A parallel transformation processes RIGF into position embeddings via another MLP, encoding the spatial relationships between patches:

$$\mathbf{E}_{\text{position}} = \text{MLP}_{\text{global}}(\text{RIGF}). \quad (7)$$

Encoder. The encoder adopts a transformer-based architecture for processing rotation-invariant features extracted from point cloud patches. The architecture consists of 12 sequential transformer blocks, each implementing an 8-head self-attention mechanism. The multi-head self-attention operation is formulated as:

$$\text{Attention}(Q, K, V) = \text{softmax}\left(\frac{QK^T}{\sqrt{d_k}}\right)V, \quad (8)$$

where the attention mechanism operates on query (Q), key (K), and value (V) matrices, with d_k denoting the dimension of keys. This formulation enables the model to capture geometric relationships across patches through learnable attention weights.

The encoder processes features progressively through its transformer blocks. The initial block receives the element-wise sum of token embeddings $\mathbf{E}_{\text{token}}$ and position embeddings $\mathbf{E}_{\text{position}}$ as input. Subsequent blocks integrate position embeddings with the processed features from their preceding blocks through residual connections. The output of the final block is a sequence of patch-level features, which can be directly fed into the decoder for reconstruction tasks. For classification or other global tasks, we further apply max-pooling and average-pooling over the sequence, and sum their results to produce a compact global representation.

Decoder. The decoder reconstructs the masked point cloud patches by leveraging the encoder’s output. Built on a transformer architecture with 4 decoding blocks, each utilizes an 8-head self-attention mechanism. The decoder processes N_v visible tokens and N_m masked tokens, where $N_m = N_p - N_v$ with N_p denoting the total number of patches. The initial masked token, represented as a d -dimensional learnable vector, is duplicated N_m times and concatenated with the visible tokens before being fed to the first decoding block. Through layer-wise self-attention operations, each block refines the embeddings by progressively capturing hierarchical geometric relationships. The final output is passed through a reconstruction head that predicts the coordinates of the masked points, thereby restoring the complete geometric structure of the point cloud.

E. Objective of Pretraining and Finetuning

Objective of Pretraining. In pretraining process, HFBRI-MAE aims to reconstruct aligned 3D coordinates within masked point cloud patches. A high masking ratio forces the model to infer missing geometric details from visible patches, focusing on meaningful geometric abstractions. The pretraining dataset consists of pre-aligned point clouds, which we directly use as $\mathbf{P}_{\text{align}}$ for the reconstruction target. The pretraining loss aims to minimize the discrepancy between predicted and aligned point clouds through the Chamfer Distance:

$$L_{\text{Chamfer}} = \sum_{x \in P_{\text{gt}}} \min_{y \in P_{\text{pred}}} \|x - y\|^2 + \sum_{y \in P_{\text{pred}}} \min_{x \in P_{\text{gt}}} \|y - x\|^2, \quad (9)$$

where P_{gt} and P_{pred} represent the ground truth and predicted aligned point clouds, respectively.

Objective of Finetuning. The pre-trained model undergoes finetuning to adapt its representations for downstream tasks. During this phase, the encoder’s output is directly fed into a task-specific prediction head. The adaptation process for classification tasks optimizes cross-entropy loss.

IV. EXPERIMENTS AND RESULTS

A. Experimental Setup

Rotation Settings. To assess the rotation invariance capability of our model, we consider three rotation configurations of point clouds. Aligned (A) represents unrotated data. Z-axis-constrained (Z) refers to rotations around the z-axis. Random (R) applies uniformly sampled rotations in the 3D space, covering all possible orientations. To evaluate rotation-invariant feature learning during pretraining, we train an SVM classifier on encoder features.

Our evaluation system utilizes a consistent notation X/Y , where X denotes the rotation applied during training (including both pretraining and subsequent finetuning or SVM training), and Y represents the rotation during testing. From the nine possible rotation combinations, we identify five critical settings. These settings demonstrate comprehensive rotation invariance performance. The A/A configuration examines performance under global orientation consistency, while

Z/Z evaluates rotation robustness with z-axis constrained rotations. A/R and Z/R assess the generalization capability from structured to random rotations. The R/R setting further demonstrates model robustness under fully random rotations. The experimental results of these five rotation settings will be presented in subsequent sections, while the complete analysis of all nine rotation settings is available in the supplementary material.

Datasets. Pretraining utilized ShapeNetCore55 [37], a diverse dataset comprising 51,300 CAD models. Finetuning was performed on ModelNet40 [38] and ScanObjectNN [39], covering synthetic and real-world scenarios, with all point clouds downsampled to 1024 points.

Downstream Tasks. The framework was evaluated on object classification, part segmentation, and few-shot learning. For classification, we used an SVM classifier on ModelNet40 when pretraining. During finetuning, we conducted separate training procedures for each dataset ModelNet40 and ScanObjectNN with their respective classification heads initialized from scratch. Part segmentation was performed on ShapeNet-Part using the category-level mean intersection-over-union (C-mIoU) metric. Few-shot learning experiments, following [40], were conducted on ModelNet40 with settings of ‘5-way 10-shot’ and ‘10-way 10-shot’.

Parameter Setup. Pretraining employed a batch size of 128, a learning rate of 0.001 with cosine decay and AdamW optimizer [41] with a weight decay of 0.05 [42], over 300 epochs. A 60% masking ratio was applied to 256 patches per point cloud, with each patch consisting of 64 points. Training was performed on a platform with an Intel Core i5-14600K CPU and an NVIDIA RTX 4090 GPU.

B. Experimental Results

Object Classification on ModelNet40. Table I presents the classification accuracy across the defined rotation settings. Non-RI methods exhibit significant performance degradation under Z/R and R/R settings, reflecting their limited robustness to rotational variations. RI methods, such as RICov++ and PaRot, deliver consistent performance but are surpassed by HFBRI-MAE.

HFBRI-MAE achieves classification accuracies exceeding 91.3% across all rotation settings. Notably, it achieves state-of-the-art performance in all settings containing rotated data, underscoring the model’s effectiveness in handling diverse rotational scenarios. Furthermore, the superiority of the finetuned model over the pretrained configuration highlights the significant benefits of task-specific optimization in enhancing performance.

Object Classification on Real-World Datasets. The ScanObjectNN-BG dataset presents significant challenges with noisy and occluded point clouds. As shown in Table II, non-RI methods experience substantial accuracy losses in A/R , Z/R , and R/R settings, reflecting their inability to handle complex real-world scenarios. While RI methods exhibit more stable performance, they are consistently outperformed by HFBRI-

TABLE I: Classification performance on ModelNet40 (A/A , A/R , Z/Z , Z/R , R/R). “RI” denotes whether the method is rotation invariance. “Pretrain” represents SVM classifier results.

Methods	RI	A/A	A/R	Z/Z	Z/R	R/R
PointNet [31]		89.2	18.2	85.9	70.2	83.1
PointNet++ [32]		90.3	22.8	89.3	72.3	85.0
DGCNN [43]		91.7	23.1	91.2	76.4	86.1
RICov [18]	✓	86.2	85.9	86.5	86.4	86.3
RI-Framework [29]	✓	89.3	89.3	89.4	89.4	89.3
Li et al. [26]	✓	89.8	90.0	90.2	90.2	90.2
OrientedMP [30]	✓	88.8	88.7	88.4	88.4	88.9
PaRot [24]	✓	91.1	90.9	90.9	91.0	90.8
RICov++ [19]	✓	91.2	90.8	91.3	91.2	91.2
SSL Methods						
PointMAE [11]		91.8	24.2	87.2	46.7	81.5
PointM2AE [12]		92.6	24.3	90.1	39.6	84.4
MaskSurf [15]		92.4	35.3	90.5	56.3	85.9
PointGPT [16]		92.6	40.5	90.5	45.2	86.2
RI-MAE [14]	✓	89.5	89.6	89.4	89.3	89.7
MaskLRF [13]	✓	91.3	90.6	91.0	91.2	91.0
HFBRI-MAE (Pretrain)	✓	89.7	89.8	89.9	89.6	89.5
HFBRI-MAE (Finetune)	✓	91.3	91.4	91.7	91.3	91.5

TABLE II: Classification performance on ScanObjectNN-BG (A/A , A/R , Z/Z , Z/R , R/R). “RI” denotes whether the method is rotation invariance. “-BG” denotes the data with background.

Methods	RI	A/A	A/R	Z/Z	Z/R	R/R
PointNet [31]		73.3	13.2	72.9	71.3	70.2
PointNet++ [32]		82.3	21.2	81.1	68.5	76.3
DGCNN [43]		82.8	31.1	81.2	69.8	80.1
RICov [18]	✓	78.4	77.9	78.5	78.8	77.8
RI-Framework [29]	✓	80.5	81.5	79.4	79.8	79.9
Li et al. [26]	✓	78.8	80.0	79.2	79.3	79.6
RICov++ [19]	✓	89.7	90.0	89.9	89.1	89.7
OrientedMP [30]	✓	76.8	78.1	77.6	76.7	77.2
PaRot [24]	✓	88.2	88.5	88.1	88.0	88.0
SSL Methods						
PointMAE [11]		90.0	26.5	85.4	42.3	86.1
PointM2AE [12]		91.2	32.8	86.3	46.3	86.3
MaskSurf [15]		91.2	29.0	86.4	39.6	89.2
PointGPT [16]		91.6	31.5	84.8	45.2	85.4
HFBRI-MAE	✓	90.1	90.5	90.0	90.3	90.0

MAE. These results demonstrate HFBRI-MAE’s robustness under diverse rotations and environmental noise.

Part Segmentation on ShapeNet. Table III demonstrates HFBRI-MAE’s superior performance in part segmentation on the ShapeNetPart dataset under Z/R rotation conditions. The model attains a C-mIoU of 79.5%, surpassing existing rotation-invariant approaches. Its effectiveness manifests particularly in complex categories such as *guitar* and *lamp*, outperforming other methods across different categories. These results validate the model’s capacity to maintain detailed semantic feature recognition under various rotational transformations.

Fig. 6 provides qualitative results of segmentation on several

TABLE III: Segmentation per class results and averaged class mIoU on ShapeNetPart dataset under Z/R, where C-mIoU stands for averaged mIoU of 16 classes.

Methods	RI	C-mIoU	aero	bag	cap	car	chair	earph.	guitar	knife	lamp	laptop	motor	mug	pistol	rocket	skate	table
PointNet [31]		37.8	40.4	48.1	46.3	24.5	45.1	39.4	29.2	42.6	52.7	36.7	21.2	55.0	29.7	26.6	32.1	35.8
PointNet++ [32]		48.3	51.3	66.0	50.8	25.2	66.7	27.7	29.7	65.6	59.7	70.1	17.2	67.3	49.9	23.4	43.8	57.6
DGCNN [43]		37.4	37.0	50.2	38.5	24.1	43.9	32.3	23.7	48.6	54.8	28.7	17.8	74.4	25.2	24.1	43.1	32.3
Li et al. [26]	✓	74.1	81.9	58.2	77.0	71.8	89.6	64.2	89.1	85.9	80.7	84.7	46.8	89.1	73.2	45.6	66.5	81.0
RICnv [18]	✓	75.3	80.6	80.0	70.8	68.8	86.8	70.3	87.3	84.7	77.8	80.6	57.4	91.2	71.5	52.3	66.5	78.4
RICnv++ [19]	✓	78.9	82.1	80.0	86.7	76.5	89.3	64.5	89.8	83.8	81.9	81.3	65.0	93.3	78.1	53.7	72.7	80.3
PaRot [24]	✓	79.2	82.7	79.2	82.3	75.3	89.4	73.9	89.1	85.6	81.0	79.5	65.3	93.9	79.2	55.0	72.4	79.5
SSL Methods																		
PointMAE [11]		34.0	36.6	31.8	38.5	31.1	33.1	31.9	37.2	37.5	39.0	35.0	25.7	43.4	32.4	29.4	31.9	29.9
PointM2AE [12]		39.6	41.1	39.3	49.5	34.6	44.7	39.2	36.0	48.6	38.4	33.0	33.5	49.9	37.7	36.2	41.4	30.6
HFBRI-MAE	✓	79.5	82.6	82.5	87.6	72.0	88.4	72.7	90.9	83.5	83.1	80.8	66.0	94.2	76.5	57.4	73.7	80.0

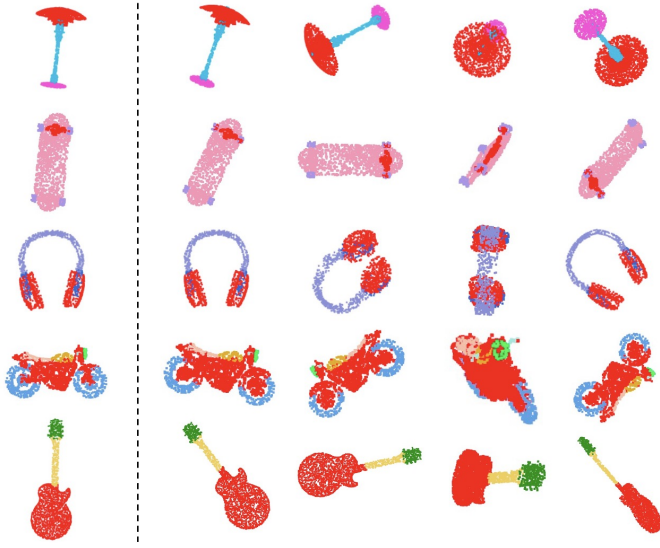


Fig. 6: Visualization of part segmentation results on the ShapeNetPart dataset under Z/R.

TABLE IV: Performance of 5-way 10-shot few-shot on ModelNetFewShot dataset.

Methods	RI	A/A	A/R	Z/Z	Z/R	R/R
PaRI-Conv [23]	✓	89.9	90.7	90.8	89.0	90.5
RICnv++ [19]	✓	87.3	87.9	87.6	87.0	87.5
PaRot [24]	✓	46.9	49.5	48.7	49.5	49.0
SSL Methods						
PointMAE [11]		96.3	52.6	85.2	56.7	87.7
PointM2AE [12]		96.8	58.1	86.3	61.4	89.1
MaskSurf [15]		96.5	50.9	84.2	55.5	90.9
PointGPT [16]		96.8	48.2	88.3	59.0	84.3
RI-MAE [14]	✓	92.2	92.3	93.1	92.7	92.5
MaskLRF [13]	✓	93.5	93.6	93.2	93.7	93.8
HFBRI-MAE	✓	93.9	94.4	93.7	93.8	93.5

challenging categories.

The visualization highlights HFBRI-MAE’s capability to preserve semantic consistency across object parts, accurately segmenting fine details like the *lamp shade* and *guitar neck*.

TABLE V: Performance of 10-way 10-shot few-shot on ModelNetFewShot dataset.

Methods	RI	A/A	A/R	Z/Z	Z/R	R/R
PaRI-Conv [23]	✓	84.6	84.6	85.2	84.5	84.0
RICnv++ [19]	✓	80.0	80.3	80.9	80.4	80.8
PaRot [24]	✓	50.9	48.3	47.8	49.5	47.7
SSL Methods						
PointMAE [11]		92.6	33.6	79.6	42.5	80.2
PointM2AE [12]		92.3	33.2	81.8	57.2	83.6
MaskSurf [15]		93.0	33.0	78.1	62.7	83.3
PointGPT [16]		92.6	30.2	80.9	60.6	79.6
RI-MAE [14]	✓	89.3	89.3	89.5	89.7	89.3
MaskLRF [13]	✓	89.2	89.0	89.3	89.2	89.5
HFBRI-MAE	✓	89.8	90.7	90.0	90.4	89.7

These results underscore the robustness and effectiveness of the proposed method in achieving consistent segmentation performance under rotational transformations.

Few-shot Classification on ModelNet40. Table IV and Table V summarize the results for the ‘5-way 10-shot’ and ‘10-way 10-shot’ settings on the ModelNetFewShot dataset. HFBRI-MAE consistently demonstrates superior performance across all rotation settings, highlighting its robust rotation-invariant capabilities. In both experiment settings, HFBRI-MAE outperforms competing methods, showcasing strong generalization and adaptability under various rotational scenarios.

C. Ablation Experiment

Mask Ratio Analysis. The mask ratio significantly impacts the model’s pretraining effectiveness by balancing visible and masked information. As shown in Table VI, a ratio of 0.6 achieves the best classification accuracy of 89.6% on ModelNet40. Lower ratios retain too much visible information, limiting feature abstraction, while higher ratios overly challenge the model, reducing performance. This underscores the importance of a balanced masking strategy.

Types of RILF. Table VII shows the effect of different RILF components on classification performance. Removing distance features (d_{px_i}) or reference point angles ($\alpha_0, \alpha_1, \alpha_2$)

TABLE VI: Performance of classification on ModelNet40 dataset with different mask ratio (Pretrain + SVM).

Mask Ratio	Average Acc.
0.3	84.6
0.5	87.0
0.8	86.7
0.6	89.7

TABLE VII: Performance of classification on ModelNet40 dataset with types of RILF.

Types of RILF	Average Acc.
Without distance features (d_{pxi})	88.7
Without reference point angles ($\alpha_0, \alpha_1, \alpha_2$)	88.1
Without inter-neighbor angles ($\phi, \beta_0, \beta_1, \beta_2$)	91.1
All	91.4

significantly reduces accuracy, highlighting their importance. In contrast, removing inter-neighbor angles ($\phi, \beta_0, \beta_1, \beta_2$) has a less pronounced impact, with accuracy dropping to 91.1%. The full feature set achieves the best performance at 91.4%, confirming the value of all features combined.

V. CONCLUSION

This paper introduced HF Bri-MAE, a novel masked auto-encoder for rotation-invariant analysis of 3D point clouds. By integrating rotation-invariant handcrafted features, the model ensures robust and consistent feature extraction across arbitrary orientations, addressing a critical limitation of conventional MAE-based approaches. Unlike conventional MAE-based approaches, HF Bri-MAE employs aligned point clouds as reconstruction targets, addressing the loss of rotational information inherent in handcrafted features. Extensive experiments on benchmark datasets demonstrate the superiority of the proposed framework in object classification, segmentation, and few-shot learning tasks. HF Bri-MAE outperforms state-of-the-art methods under various rotation settings, showcasing its adaptability and effectiveness in both synthetic and real-world scenarios.

REFERENCES

- [1] Y. Guo, H. Wang, Q. Hu, H. Liu, L. Liu, and M. Bennamoun, "Deep learning for 3d point clouds: A survey," in *IEEE Transactions on Pattern Analysis and Machine Intelligence*, 2020, 43(12), pp. 4338-4364.
- [2] Y. Cui et al., "Deep learning for image and point cloud fusion in autonomous driving: A review," in *IEEE Transactions on Intelligent Transportation Systems*, 2021, 23(2), pp. 722-739.
- [3] Q. Cheng, P. Sun, C. Yang, Y. Yang, and P. X. Liu, "A morphing-based 3D point cloud reconstruction framework for medical image processing," in *Computer Methods and Programs in Biomedicine*, 2020, 193, p. 105495.
- [4] J. Yu et al. "3d medical point transformer: Introducing convolution to attention networks for medical point cloud analysis," arXiv preprint arXiv:2112.04863 (2021).
- [5] H. Duan, P. Wang, Y. Huang, G. Xu, W. Wei, and X. Shen, "Robotics dexterous grasping: The methods based on point cloud and deep learning," in *Frontiers in Neurorobotics*, 2021, 15, p. 658280.
- [6] S. Xie, G. Jiatao, D. Guo, C. R. Qi, L. Guibas, and O. Litany, "Point-Contrast: Unsupervised pre-training for 3D point cloud understanding," in *ECCV*, 2020, pp. 574-591.

- [7] M. Afham, I. Dissanayake, D. Dissanayake, A. Dharmasiri, K. Thilakarathna, and R. Rodrigo, "CrossPoint: Self-supervised cross-modal contrastive learning for 3D point cloud understanding," in *CVPR*, 2022, pp. 9902-9912.
- [8] H. Liang et al., "Exploring geometry-aware contrast and clustering harmonization for self-supervised 3D object detection," in *ICCV*, 2021, pp. 3293-3302.
- [9] Y. Yang, C. Feng, Y. Shen, and D. Tian, "FoldingNet: Point cloud auto-encoder via deep grid deformation," in *CVPR*, 2018, pp. 206-215.
- [10] J. Yang, P. Ahn, D. Kim, H. Lee, and J. Kim, "Progressive seed generation auto-encoder for unsupervised point cloud learning," in *ICCV*, 2021, pp. 6413-6422.
- [11] Y. Pang, W. Wang, F. E. Tay, W. Liu, Y. Tian, and L. Yuan, "Masked autoencoders for point cloud self-supervised learning," in *ECCV*, 2022, pp. 604-621.
- [12] R. Zhang et al., "Point-M2AE: Multi-scale masked autoencoders for hierarchical point cloud pre-training," in *NeurIPS*, 2022, 35, pp. 27061-27074.
- [13] T. Furuya, "MaskLRF: Self-supervised Pretraining via Masked Autoencoding of Local Reference Frames for Rotation-invariant 3D Point Set Analysis," in *IEEE Access*, 2024.
- [14] K. Su et al., "RI-MAE: Rotation-Invariant Masked AutoEncoders for Self-Supervised Point Cloud Representation Learning," in *arXiv preprint*, 2024, arXiv:2409.00353.
- [15] Y. Zhang, J. Lin, C. He, Y. Chen, K. Jia, and L. Zhang, "Masked surfel prediction for self-supervised point cloud learning," in *arXiv preprint*, 2022, arXiv:2207.03111.
- [16] G. Chen, M. Wang, Y. Yang, K. Yu, L. Yuan, and Y. Yue, "Point-GPT: Auto-regressively generative pre-training from point clouds," in *NeurIPS*, 2024, vol. 36.
- [17] D. Zhang, J. Yu, T. Xue, C. Zhang, D. Liu, and W. Cai, "Enhancing Robustness to Noise Corruption for Point Cloud Recognition via Spatial Sorting and Set-Mixing Aggregation Module," in *ACCV*, 2024, pp. 4205-4222.
- [18] Z. Zhang, B. S. Hua, W. David, Rosen, and S. K. Yeung, "Rotation invariant convolutions for 3D point clouds deep learning," in *3DV*, 2019, pp. 204-213.
- [19] Z. Zhang, B. S. Hua, and S. K. Yeung, "RICov++: Effective rotation invariant convolutions for 3D point clouds deep learning," in *International Journal of Computer Vision*, 2022, 130(5), pp. 1228-1243.
- [20] Z. Zhang, B. S. Hua, W. Chen, Y. Tian, and S. K. Yeung, "Global context aware convolutions for 3D point cloud understanding," in *3DV*, 2020, pp. 210-219.
- [21] C. Zhao, J. Yang, X. Xiong, A. Zhu, X. Cao, and X. Li, "Rotation invariant point cloud analysis: Where local geometry meets global topology," in *Pattern Recognition*, 2022, 127, p. 108626.
- [22] J. Yu, C. Zhang, and W. Cai, "Rethinking rotation invariance with point cloud registration," in *AAAI*, 2023, vol. 37, No. 3, pp. 3313-3321.
- [23] R. Chen, and C. Yang, "The devil is in the pose: Ambiguity-free 3D rotation-invariant learning via pose-aware convolution," in *CVPR*, 2022, pp. 7472-7481.
- [24] D. Zhang, J. Yu, C. Zhang, and W. Cai, "PaRot: Patch-wise rotation-invariant network via feature disentanglement and pose restoration," in *AAAI*, 2023, vol. 37, no. 3, pp. 3418-3426.
- [25] S. Kim, J. Park, and B. Han, "Rotation-invariant local-to-global representation learning for 3D point cloud," in *NeurIPS*, 2020, 33, pp. 8174-8185.
- [26] F. Li, K. Fujiwara, F. Okura, and Y. Matsushita, "A closer look at rotation-invariant deep point cloud analysis," in *ICCV*, 2021, pp. 16218-16227.
- [27] A. Poulernard, and J.G. Leonidas, "A functional approach to rotation equivariant non-linearities for Tensor Field Networks," in *CVPR*, 2021, pp. 13174-13183.
- [28] F. Fuchs, D. Worrall, V. Fischer, and M. Welling, "SE(3)-Transformers: 3D roto-translation equivariant attention networks," in *NeurIPS*, 2022, 33, pp. 1970-1981.
- [29] X. Li et al., "A rotation-invariant framework for deep point cloud analysis," in *IEEE Transactions on Visualization and Computer Graphics*, 2021, pp. 4503-4514.
- [30] S. Luo, J. Li, J. Guan, Y. Su, C. Cheng, J. Peng, and J. Ma, "Equivariant point cloud analysis via learning orientations for message passing," in *CVPR*, 2022, pp. 18932-18941.

- [31] C. R. Qi, H. Su, K. Mo, and L. J. Guibas, "PointNet: Deep learning on point sets for 3D classification and segmentation," in *CVPR*, 2017, pp. 652–660.
- [32] C. R. Qi, H. Su, K. Mo, and L. J. Guibas, "PointNet++: Deep hierarchical feature learning on point sets in a metric space," in *NeurIPS*, 2017, vol. 30.
- [33] G. Qian, Y. Li, H. Peng, J. Mai, H. Hammoud, M. Elhoseiny and B. Ghanem, "PointNetXt: Revisiting PointNet++ with improved training and scaling strategies," in *NeurIPS*, 2022, vol. 35, pp. 23192–23204.
- [34] M. Guo, J. Cai, Z. Liu, T. Mu, R. Martin and S. Hu, "PCT: Point cloud transformer," in *Computational Visual Media*, 2021, vol. 7, pp. 187–199.
- [35] T. Xiang, C. Zhang, Y. Song, J. Yu and W. Cai, "Walk in the cloud: Learning curves for point clouds shape analysis," in *ICCV*, 2021, pp. 915–924.
- [36] H. Zhao, J. Li, J. Jia, H. T. Philip and K. Vladlen, "Point transformer," in *ICCV*, 2021, pp. 16259–16268.
- [37] A.X. Chang, T. Funkhouser, L. Guibas, "ShapeNet: An information-rich 3D model repository," in *arXiv preprint*, 2015, arXiv:1512.03012.
- [38] Z. Wu et al., "3D ShapeNets: A deep representation for volumetric shapes," in *CVPR*, 2015, pp. 1912–1920.
- [39] M. A. Uy, Q. H. Pham, B. S. Hua, T. Nguyen, and S. K. Yeung, "Revisiting point cloud classification: A new benchmark dataset and classification model on real-world data," in *ICCV*, 2019, pp. 1588–1597.
- [40] C. Sharma, and M. Kaul, "Self-supervised few-shot learning on point clouds," in *NeurIPS*, 2020, pp. 7212–7221.
- [41] I. Loshchilov, and F. Hutter, "Fixing weight decay regularization in Adam," in *arXiv preprint*, 2017, arXiv:1711.05101.
- [42] I. Loshchilov, "SGDR: Stochastic gradient descent with warm restarts," in *arXiv preprint*, 2016, arXiv:1608.03983.
- [43] Y. Wang, Y. Sun, Z. Liu, S. E. Sarma, M. M. Bronstein, and J. M. Solomon, "Dynamic graph CNN for learning on point clouds," in *ACM Transactions on Graphics (tog)*, 2019, 38(5), pp. 1–12.

A. RILF Details

RILF. RILF consists of three types of features that encode invariant geometric relationships within each patch.

The first type comprises distance-based features, specifically the Euclidean distance $d_{pxi} = |x_i - p|$ between reference point p and its i -th neighbor x_i , which captures essential local spatial relationships.

The second type captures angular relationships with respect to the reference point through three critical angles: the polar angle $\alpha_0 = \angle(LRA_{x_i}, \overrightarrow{x_i p})$ between the Local Reference Axis (LRA) of x_i and the vector from x_i to p ; the azimuthal angle $\alpha_1 = \angle(LRA_p, \overrightarrow{x_i p})$ between the reference point’s LRA and the vector $\overrightarrow{x_i p}$; and a signed angle $\alpha_2 = S_a \cdot \angle(LRA_{x_i}, LRA_p)$ between the LRAs of p and x_i , where S_a preserves rotational directionality.

The third type encompasses geometric relationships among neighboring points, including the angle $\phi = \angle(\overrightarrow{x_{i+1} p}, \overrightarrow{x_i p})$ between consecutive neighbor vectors, the azimuthal angle $\beta_0 = \angle(LRA_{x_i}, \overrightarrow{x_i x_{i+1}})$ between a neighbor’s LRA and the vector to the next neighbor, the polar angle $\beta_1 = \angle(LRA_{x_{i+1}}, \overrightarrow{x_i x_{i+1}})$ and a signed angle $\beta_2 = S_b \cdot \angle(LRA_{x_i}, LRA_{x_{i+1}})$ between consecutive LRAs.

RIGF. RIGF contains distance-based features and angular features.

The distance-based features include three key measurements: the distance to origin $d_{pi} = |p_i|$ for each reference point p_i , providing global positioning; the distance to geometric median $d_{pmi} = |p_i - m_i|$ where m_i represents the geometric median of the neighborhood ball, capturing local density information; and the distance $d_{smi} = |s_i - m_i|$ between the boundary point s_i and the geometric median, encoding the spatial extent of local neighborhoods.

The angular features comprise two principal measurements: $\alpha_i = \angle(\overrightarrow{p_i m_i}, \overrightarrow{s_i m_i})$, measuring the angle between the reference point and boundary point vectors from the geometric median, and $\beta_i = \angle(\overrightarrow{p_i s_i}, \overrightarrow{m_i s_i})$, capturing the angular relationship between the boundary point and geometric median vectors from the reference point perspective. These features together provide a complete characterization of the point cloud’s geometry while maintaining rotation invariance at both local and global scales.

B. Embedding Details

Token Embedding. As shown in Fig. 7, the token embedding pathway processes eight-dimensional local rotation-invariant features with an initial dimension of $B \times N \times K \times 8$, where B represents the batch size, N indicates the number of patches, and K denotes the number of points in each patch. This pathway implements a sophisticated multi-layer perceptron (MLP) structure, where each MLP block comprises three essential components: a convolution layer for feature transformation, batch normalization for training stability, and ReLU activation for non-linearity.

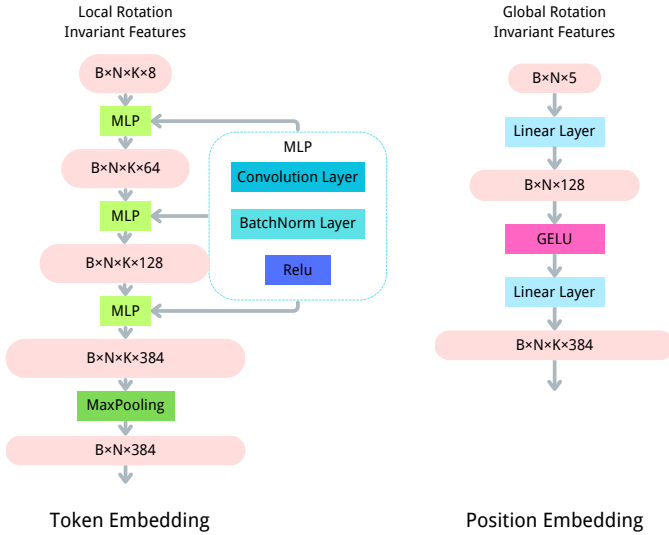


Fig. 7: Embedding architecture overview. The left branch shows the token embedding pathway, which processes local rotation-invariant features through multiple MLP blocks (consisting of convolution, batch normalization, and ReLU activation) and a final max pooling operation. The right branch illustrates the position embedding pathway, which transforms global rotation-invariant features through a simpler architecture of linear layers and GELU activation. Both pathways produce embeddings of compatible dimensions ($B \times N \times 384$) for subsequent transformer processing.

The network architecture progressively expands the feature dimensionality through three sequential MLP blocks. The first block transforms the initial 8-dimensional features to 64 dimensions ($B \times N \times K \times 64$), followed by a second block that further expands to 128 dimensions ($B \times N \times K \times 128$). The final MLP block produces a 384-dimensional representation ($B \times N \times K \times 384$). To consolidate the point-wise features within each patch, a max pooling operation is applied across the K dimension, resulting in the final token embedding of dimension $B \times N \times 384$.

Position Embedding. The position embedding pathway processes five-dimensional global rotation-invariant features, starting with an input dimension of $B \times N \times 5$. In contrast to the token embedding pathway, this architecture employs a more streamlined structure optimized for global spatial information. The pathway begins with a linear layer that expands the feature dimension from 5 to 128, producing an intermediate representation of $B \times N \times 128$. This intermediate representation then passes through a GELU activation function, introducing non-linearity while maintaining smooth gradients. A final linear layer transforms the features to match the token embedding dimension, producing a position embedding of $B \times N \times K \times 384$. This simpler architecture effectively captures global spatial relationships while maintaining dimensional compatibility with the token embeddings for subsequent transformer processing.

C. Network Architecture for Downstream Tasks

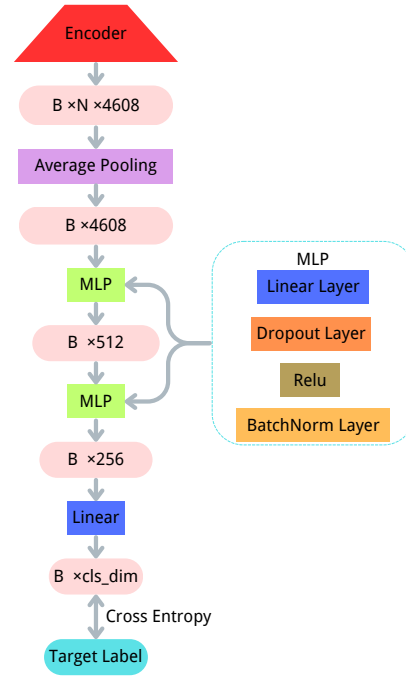


Fig. 8: Classification head architecture. The network processes encoder outputs through average pooling and progressive dimensionality reduction via MLP blocks, culminating in class-specific predictions.

Classification Head. As illustrated in Fig. 8, our classification head architecture efficiently processes the encoder’s output features ($B \times N \times 4608$) through a series of carefully designed transformations. The processing begins with an average pooling operation across the patch dimension, consolidating patch-wise features into a global $B \times 4608$ representation. This pooled feature vector then passes through two sequential MLP blocks, each comprising a linear layer, dropout, ReLU activation, and batch normalization. These MLP blocks progressively reduce the feature dimensionality from 4608 to 512, and then to 256, before a final linear layer maps the features to the target classification dimension ($B \times \text{cls_dim}$). This architecture effectively distills the essential geometric information from the encoder’s output while maintaining robust classification performance.

Segmentation Head. As shown in Fig. 9, our segmentation head processes the encoder’s multi-scale features through a carefully designed architecture that combines global contextual information with point-wise predictions. The network begins by processing the encoder output of dimension $B \times N \times 384$ through transformer blocks, which expand the feature dimension to $B \times N \times 1152$, providing richer geometric representations.

The expanded features then flow through three parallel branches. Two branches perform average and max pooling operations respectively, both producing features of dimension $B \times 1152 \times P$, where P represents the number of points. The third branch processes classification labels to generate point-

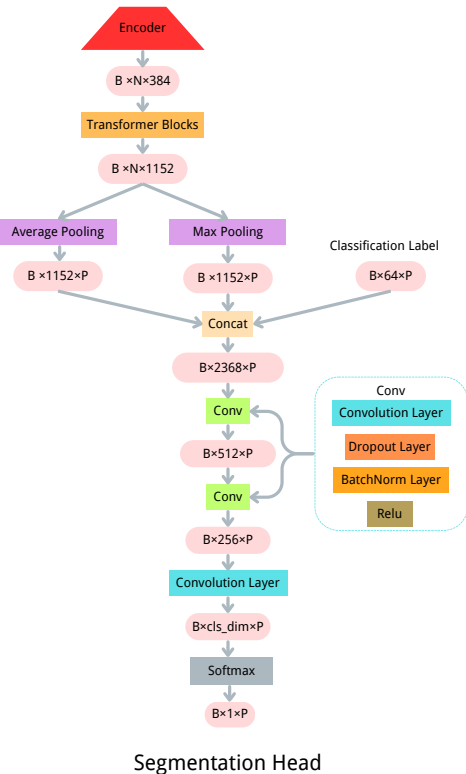


Fig. 9: Architecture of the segmentation head. The diagram illustrates the flow from encoder features through parallel pooling branches and classification label integration, followed by progressive feature refinement via convolutional blocks, culminating in point-wise segmentation predictions.

wise label features of dimension $B \times 64 \times P$. These three streams are concatenated to form a comprehensive feature representation of dimension $B \times 2368 \times P$, effectively combining global contextual information with local geometric details.

This concatenated feature tensor then undergoes progressive refinement through a series of convolutional blocks. Each convolutional block consists of a convolution layer, followed by batch normalization, ReLU activation, and dropout for regularization. The first convolution reduces the feature dimension to $B \times 512 \times P$, followed by a second convolution that further reduces it to $B \times 256 \times P$. A final convolution layer maps the features to the target segmentation dimension $B \times \text{cls_dim} \times P$, where cls_dim represents the number of segmentation classes. The architecture concludes with a softmax operation that produces point-wise segmentation probabilities of dimension $B \times 1 \times P$.

D. More Ablation Experiments

Completed Classification Results. Tables XI, XII, and XIII present the classification results of various methods across nine rotation settings on the ModelNet40, ScanObjectNN, and OmniObject3D datasets, respectively. These datasets provide a comprehensive evaluation of the rotation-invariant capabilities of the proposed HFBR-MAE framework.

TABLE VIII: Performance of classification on ModelNet40 dataset with different numbers of patches and points per patch (Pretrain + SVM).

Number of Patches	Points Per Patch	Average Acc.
128	16	83.0
128	64	86.3
256	16	85.4
256	32	88.2
512	32	87.1
512	64	84.7
256	64	89.6

TABLE IX: Performance of classification on ModelNet40 dataset with different finetune strategies (Pretrain + SVM).

Finetune Strategy	Test Dataset	Train Dataset
All Parameters	91.0	99.3
Only Cls-head	91.4	92.1

TABLE X: Performance of classification on ModelNet40 dataset with different global features.

Global Representations	Average Acc.
RIConv++	90.8
ReLRF	90.0
RIConv++ concat Grif	89.9
Ours	91.4

Patch Count and Point Density. The number of patches and points per patch directly influences the model’s ability to capture local and global geometric details. Table VIII shows that the configuration with 256 patches and 64 points per patch achieves the best performance, with an accuracy of 89.6% on ModelNet40. Smaller patch counts with fewer points result in insufficient feature coverage, while excessive patch numbers lead to redundancy and decreased generalization. This demonstrates the importance of selecting an appropriate balance between patch granularity and local detail representation.

Finetuning Strategies. The influence of different finetuning strategies on classification accuracy was also evaluated. As shown in Table IX, our method achieves the highest average accuracy when combining supervised finetuning with our pretrained rotation-invariant encoder, reaching 91.5% on ModelNet40. This demonstrates the strong transferability of the features learned during pretraining and their adaptability to downstream tasks.

Global Rotation-Invariant Representations. We compared various global rotation-invariant representations extraction strategies, including RIConv++, ReLRF and a hybrid approach combining RIConv++ with our handcrafted representations. As shown in Table X, RiHanFa-MAE achieves the highest accuracy of 89.6%, surpassing both RIConv++ and ReLRF individually. This result validates the effectiveness of our handcrafted global features in capturing robust and rotation-invariant representations.

TABLE XI: Classification performance on ModelNet40. “RI” denotes whether the method is rotation invariance.

Methods	RI	A/A	A/Z	A/R	Z/A	Z/Z	Z/R	R/A	R/Z	R/R
PointNet		89.2	30.8	18.2	45.7	85.9	70.2	78.3	77.1	83.1
PointNet		90.3	36.0	22.8	48.2	89.3	72.3	81.7	81.2	85.0
DGCNN		91.7	38.5	23.1	50.7	91.2	76.4	83.8	84.5	86.1
RIConv	✓	86.2	86.4	85.9	86.3	86.5	86.4	86.4	86.5	86.3
RI-Framework	✓	89.3	89.0	89.3	89.3	89.4	89.4	89.2	89.2	89.3
Li et al.	✓	89.8	90.3	90.0	90.4	90.2	90.2	90.1	90.0	90.2
OrientedMP	✓	88.8	88.3	88.7	88.3	88.4	88.4	88.6	88.8	88.9
PaRot	✓	91.1	91.0	90.9	90.8	90.9	91.0	90.8	90.9	90.8
RIConv++	✓	91.2	91.1	90.8	91.4	91.3	91.2	91.2	91.7	91.2
SSL Methods										
PointMAE		91.8	39.2	24.2	86.4	87.2	46.7	79.6	80.3	81.5
PointM2AE		92.6	39.8	24.3	91.5	92.1	39.6	88.4	89.1	89.4
MaskSurf		92.4	50.4	35.3	63.9	90.5	56.3	83.3	83.1	85.9
PointGPT		92.6	55.0	40.5	68.3	90.5	45.2	84.6	84.5	86.2
RI-MAE	✓	89.5	89.2	89.6	89.9	89.4	89.3	89.5	89.3	89.7
MaskLRF	✓	91.3	90.7	90.6	91.0	91.0	91.2	91.3	91.3	91.0
HFBRI-MAE (pretrain+svm)	✓	89.7	89.7	89.8	89.6	89.9	89.6	89.9	89.8	89.5
HFBRI-MAE (finetune)	✓	91.3	91.5	91.4	91.6	91.7	91.3	91.4	91.8	91.5

TABLE XII: Classification performance on ScanObjectNN-BG. “RI” denotes whether the method is rotation invariance. “-BG” denotes the data with background.

Methods	RI	A/A	A/Z	A/R	Z/A	Z/Z	Z/R	R/A	R/Z	R/R
PointNet		73.3	20.3	13.2	31.5	72.9	71.3	68.0	70.9	70.2
PointNet++		82.3	31.3	21.2	45.7	81.1	68.5	78.5	76.9	76.3
DGCNN		82.8	36.1	31.1	46.8	81.2	69.8	81.8	80.5	80.1
RIConv	✓	78.4	77.8	77.9	79.1	78.5	78.8	76.6	77.1	77.8
RI-Framework	✓	80.5	79.9	81.5	79.3	79.4	79.8	80.0	80.3	79.9
Li et al.	✓	78.8	79.5	80.0	79.4	79.2	79.3	78.9	79.0	79.6
RIConv++	✓	89.7	89.3	90.0	88.9	89.9	89.1	88.7	89.5	89.7
OrientedMP	✓	76.8	77.2	78.1	77.7	77.6	76.7	76.6	78.8	77.2
PaRot	✓	88.2	87.9	88.5	88.9	88.1	88.0	89.1	88.7	88.0
SSL Methods										
PointMAE		90.0	37.9	26.5	88.1	85.4	42.3	84.1	85.3	86.1
PointM2AE		91.2	50.0	32.8	87.9	86.3	46.3	87.4	88.0	86.3
MaskSurf		91.2	41.3	29.0	84.6	86.4	39.6	88.8	87.3	89.2
PointGPT		91.6	46.7	31.5	89.9	84.8	45.2	86.7	83.9	85.4
HFBRI-MAE	✓	89.5	90.2	90.5	90.1	90.0	90.3	89.4	90.8	90.0

TABLE XIII: Classification performance on OmniObject3D. “RI” denotes whether the method is rotation invariance.

Methods	RI	A/A	A/Z	A/R	Z/A	Z/Z	Z/R	R/A	R/Z	R/R
PaRI-Conv	✓	68.1	68.5	68.2	67.8	68.1	67.9	68.7	68.3	67.9
RIConv++	✓	71.2	70.9	70.9	71.4	71.5	70.8	71.6	70.8	71.1
PaRot	✓	71.7	70.9	70.7	70.8	71.1	70.5	70.8	71.3	70.9
SSL Methods										
PointMAE		71.4	17.8	9.1	72.1	71.9	42.3	70.1	71.0	70.5
PointM2AE		72.1	20.3	13.4	71.9	73.3	46.5	72.4	72.0	72.3
MaskSurf		72.3	18.5	11.2	71.6	71.2	43.0	71.8	72.2	71.7
PointGPT		71.7	20.3	9.7	65.7	62.5	21.7	58.2	56.3	57.9
HFBRI-MAE	✓	71.8	72.0	72.3	72.2	71.8	71.7	72.1	71.7	72.0